THE JOURNAL OF PHYSICAL CHEMISTRY C
A JOURNAL OF THE AMERICAN CHEMICAL SOCIETY

pubs.acs.org/JPCC

Article

Catalytic Conversion of CO and H_2 into Hydrocarbons on the Cobalt Co(111) Surface: Implications for the Fischer–Tropsch Process

David Santos-Carballal,* Abdelaziz Cadi-Essadek, and Nora H. de Leeuw*

Cite This: *J. Phys. Chem. C* 2021, 125, 11891–11903

Read Online

ACCESS | Metrics & More | Article Recommendations | Supporting Information

ABSTRACT: The Fischer–Tropsch (FT) process consists of the reaction of a synthesis gas (syngas) mixture containing carbon monoxide (CO) and hydrogen (H_2), which are polymerized into liquid hydrocarbon chains, often using a cobalt catalyst, although the mechanistic pathway is not yet fully understood. Here, we have employed unrestricted density functional theory calculations with a Hubbard Hamiltonian and long-range dispersion corrections [DFT+*U*–D3–(BJ)] to investigate the reaction of syngas and the selectivity toward the hydrocarbons formed on the cobalt Co(111) surface. The single CO and dissociated H_2 molecules prefer to adsorb at two different types of trigonal surface sites, and we discuss how the interatomic distances, fundamental vibrational modes, charge transfers, surface-free energies, and work functions are modified by the adsorbates. The coadsorption of the syngas molecules in close proximity provides enough energy for the system to cross the saddle points on the minimum energy pathway (MEP), leading to the catalytic hydrogenolysis of the C–O bond. The adsorbed CO, alongside the intermediates CH and OH, are further stabilized when the ratio of equilibrium coverage (C) is $C_H/C_{CO,CH,OH} > 6{:}1$ under the temperature conditions required for the FT process. We propose several mechanistic pathways to account for the formation of ethane (C_2H_6), as a model for long-chain hydrocarbons, as well as methane (CH_4) which is an undesirable product. The MEPs for these processes show that the coupling of the C–C bond followed by hydrogenation is the most favorable process, which takes precedence over the production of CH_4. The termination reaction suggests that water (H_2O) remains weakly physisorbed to the surface, allowing the reutilization of its catalytic site. The simulated fundamental vibrational frequencies and scanning tunneling microscopy images of the surface-bound intermediates are in agreement with the available experimental data. Our findings are important in the interpretation of the elementary steps of the FT process on the Co(111) surface.

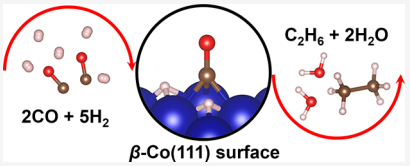

1. INTRODUCTION

The Fischer–Tropsch (FT) process is the most relevant method used industrially for the polymerization of one-carbon (C1) molecules into valuable products that can be used as chemicals or fuels.[1−8] FT is an indirect liquefaction process that uses a synthesis gas as a chemical feedstock[9−11] and a transition metal as the catalyst.[12−16] The so-called syngas comprises carbon monoxide (CO) and molecular hydrogen (H_2) produced by the gasification of coal,[17−20] organic waste, and biomass,[17−19,21,22] or by reforming natural gas.[17,23,24] Straight-chain (oxygenated) hydrocarbons of high purity, containing between 10 and 20 carbon atoms, are produced which are commercially valuable as synthetic motor-gasoline (petrol)[25,26] as well as diesel[25,27] and high-performance jet fuels.[28−30] The combustion of these synfuels is very clean, thus causing negligible adverse health and environmental impacts compared to conventional fuels, which emit large amounts of harmful pollutants, including sulfur oxides (SO_x),[30−32] nitrogen oxides (NO_x),[32] and particulate matter.[30−33] FT synfuels, in particular those derived from biomass, have attracted great renewed attention as a sustainable route to achieve a net zero-carbon future and mitigate global warming by 2050.[34−37]

It is generally accepted that transforming syngas into (oxygenated) hydrocarbons involves a series of concatenated elementary steps as well as surface-bound intermediates and byproducts that are difficult to detect.[38] The carbon chain growth is one of the most intriguing aspects of the FT mechanism, which consists of (1) dissociative adsorption of H_2; (2) molecular adsorption of CO; (3) dissociation of the C–O bond; (4) formation and desorption of H_2O; (5) formation of the methylene $-CH_2-$ radical; and (6) formation of the C–C bond.[38] Despite strong evidence supporting CO dissociation and stepwise hydrogenation followed by $-CH_2-$ polymerization,[39,40] alternative chain propagation mechanisms include ethene[41,42] and CO insertion,[43−45] depending on the reaction conditions and desired type of products. Spatial constrains favor terminal alkyl intermediates fixed to the catalyst surface site,[46,47] which controls the selectivity toward straight chain hydrocarbons.[48−50] Moreover, the principle of selective inhibition developed by Schulz and co-workers posits that dissociative desorption of terminal alkyl species forming α-olefins is more likely than addition of one H atom to form

Received: January 11, 2021
Revised: April 28, 2021
Published: May 28, 2021

paraffins.[51−53] One of the major challenges of the FT process is to control the selectivity toward the wide distribution of products, which obeys the Anderson−Schulz−Flory probability distribution.[54,55] Since the FT process is rather unselective, producing hydrocarbons ranging from methane gas to C_{80} solid paraffin waxes, several approaches have been used extensively to narrow the hydrocarbon fractions. The multistage oligomerization of the low molecular weight α-olefins is practiced in the industry to maximize the gasoline yield, whereas the hydrocracking of the paraffin wax to diesel adds further commercial value to the products of the FT synthesis.[27] In contrast, bifunctional catalysts combining an FT-active Co phase embedded into the cavities of an acid mesoporous catalyst are used for the direct selective synthesis of hydrocarbons[56−58] as well as core−shell nanoreactors, characterized by hollow nanospheres based on an inorganic or organic matrix encapsulating an FT-active metal.[59−61]

Transition metals are the major components of conventional FT catalysts used for industrial applications. Ruthenium is the most active metal known, catalyzing the synthesis of polymethylene at the lowest reaction temperature and without requiring any promoter, but its limited abundance and high price prevent large-scale use in chemical plants.[12,14,62−65] Nickel is the most active for hydrogenation reactions and as a result shows high selectivity for methane formation, which has a low commercial value.[66] Iron is a very versatile catalyst, as its selectivity can be tailored using various additives and reaction conditions to produce α-olefins[67−71] or paraffin wax.[13,72−76] However, Fe also displays activity for the water−gas shift reaction (WGSR),[77−81] which is undesirable for H_2-rich syngas mixtures, as the H_2O poisons the catalyst surface, reducing the FT conversion yields.[78,82,83] In contrast, cobalt exhibits negligible activity for the competitive and unwanted WGSR,[84] making it a suitable catalysts for the FT synthesis.[85−90] Co is used to produce paraffin wax, due to the surface properties of this metal, which allows the readsorption and insertion of α-olefins into the surface intermediates.[15,91]

Co is a very stable catalyst that has a high selectivity for straight chain alkanes.[92] This metal displays the best catalytic activity in the pressure range of 10−60 bars and at temperatures between 473 and 573 K.[93] Under FT operating conditions, evidence from in situ extended X-ray adsorption fine structure has shown that the catalyst remains in the zero-valence state.[94] It has been suggested that the slowest and, therefore, rate-determining step of the catalytic process on Co is the vicinal site reduction of a carbon-containing intermediate by atomic H.[93] Improving the dispersion of the Co catalyst by reducing the size of the supported material is a known route to enhance the selectivity and catalytic activity during the FT process.[95] The catalytic activity of the Co(111) surface has been the focus of intense scrutiny[96,97] since it has shown to be highly stable under the FT conditions.[98]

In this paper, we have used density functional theory (DFT) simulations to investigate the conversion of syngas into hydrocarbons of different chain lengths on the Co(111) surface. We have studied the single molecule adsorption and coadsorption of the reactants and discuss the impact on the interatomic distances, fundamental vibrational modes, charge transfers, atomic magnetic moments, surface free energies, and surface work function. We have also analyzed the role of several partial pressures of H on the thermodynamic stability of the Co(111) surface in the presence of various intermediate chemical species. We have used the climbing image nudged elastic band (cNEB) method to investigate the reaction profiles for (i) the activation of the surface-bound H and CO, (ii) the combination of CH and H into CH_4 and C_2H_6, and (iii) the formation of H_2O and CO_2, which is essential to understand the chemistry of the FT process over cobalt. We also predict the simulated infrared (IR) spectra and scanning tunneling microscopy (STM) images for the intermediates of the reaction mechanisms that we have examined for comparison with future experiments.

2. COMPUTATIONAL METHODS

2.1. Calculation Details. We have performed spin-polarized DFT calculations using the Vienna ab initio simulation package (VASP).[99−102] The exchange correlation potential was described using the Perdew, Burke, and Ernzerhof functional within the generalized gradient approximation.[103,104] The core levels were defined up to and including 3*p* and 1*s* for the Co and the nonmetal C and O atoms, respectively, whereas the electron in the H atom was treated as a valence state. The frozen ions and their interaction with the valence electrons were simulated within the projected augmented wave framework.[105,106] The Kohn−Sham valence states were expanded using a plane-wave basis set with a cut-off of 500 eV for the kinetic energy. We have applied the simplified rotationally invariant version[107] of the Hubbard Hamiltonian,[108] where we have used the unified value of U_{eff} = 3.0 eV to account for the delocalized nature of the Co 3*d* electrons. This choice of cut-off and on-site Coulomb correction values was appropriate to describe different phases of metallic Co as well as their oxides and surfaces.[109,110] The structures were relaxed using the conjugate-gradient method until all forces on the atoms were less than 0.01 eV $Å^{-1}$. The electronic density optimization was stopped when the total energy difference between two consecutive self-consistent loop steps was below 10^{-5} eV. In order to accurately describe the long-range dispersion interactions, we have adopted the empirical correction method with the Becke−Johnson damping presented by Grimme and co-workers [D3−(BJ)],[111,112] which has been proven reliable in the simulation of surface properties of various materials.[109,113−117]

2.2. Surface and Molecular Models. The (111) surface was investigated using the periodic $p(3 \times 3)$ supercell, which was created from the bulk of Co using METADISE.[118] A vacuum of 18 Å was added in the direction perpendicular to the surface to prevent interaction with the periodically repeated images. We considered four atomic layers for the simulation of the (111) surface slab, with an area of 48.318 $Å^2$. The atoms in the two topmost layers were allowed to relax during geometry optimizations, to mimic the surface, while those atoms in the remaining two bottom layers were kept at their optimized bulk positions. The Brillouin zone of the surface was sampled using a Γ-centered Monkhorst−Pack mesh of 5 × 5 × 1 *k*-points[119] and integrated using the order 1 of the method by Methfessel and Paxton[120] with 0.2 eV for the width of the smearing. The Methfessel and Paxton method ensured that the variational quantity, that is, the electronic entropy, vanished during the estimation of the electronic partial occupancies.[121] However, we employed the tetrahedron method with Blöchl corrections[122] for the simulation of accurate energies as well as the electronic and magnetic properties. Energy convergence within 1 meV per atom was further tested for the simulation supercell using different vacuum thicknesses as well as various numbers of total and

https://doi.org/10.1021/acs.jpcc.1c00254
J. Phys. Chem. C 2021, 125, 11891−11903

relaxed atomic layers. Dipole corrections were also included perpendicular to the surface plane to compensate for any dipole created by the chemical species added on the relaxed side of the slab and to enhance the electronic convergence.[123,124]

The isolated CO and H_2 molecules were modeled in a periodic box of 14 × 15 × 16 Å^3 to ensure negligible interaction with their images in the neighboring cells. The Gaussian scheme was used to determine the electronic partial occupancies during geometry optimizations and energy calculations, sampling only the Γ point of the Brillouin zone.

The effective Bader atomic charges were obtained using an improved grid of charge density values without lattice bias,[125−127] whereas the magnetic moments were integrated within the same atomic basins. The work function (Φ), which is the minimum thermodynamic work required for an electron to leave the Co(111) surface, was calculated as $\Phi = E_{vac} - E_F$, where E_{vac} is the potential at the vacuum and E_F is the Fermi level of the slab. The STM images were simulated using the Tersoff−Hamann method[128] in the implementation of Vanpoucke and Brocks.[129] The wavenumbers of the fundamental vibrational modes were determined using the central finite differences approach, by allowing each atom to move by a small displacement in the three Cartesian directions. The saddle points and minimum energy pathways (MEPs) between initial and final states were simulated using the cNEB method.[130,131] We used five images to model the MEP, which were optimized globally by means of the limited-memory Broyden−Fletcher−Goldfarb−Shanno method.[132,133] The saddle points were characterized by a single imaginary frequency along the reaction coordinate, which were determined using the central finite difference method.

2.3. Surface Energy Diagrams. The surface energies for the slab before (γ_u) and after relaxation (γ_r) were evaluated as

$$\gamma_u = \frac{E_u - n_b E_b}{2A} \tag{1}$$

$$\gamma_r = \frac{E_r - n_b E_b}{A} - \gamma_u \tag{2}$$

where E_u, E_r, and E_b are the energies of the unrelaxed slab, the half-relaxed slab, and one Co atom in the bulk, respectively. n_b and A are the number of Co atoms in the supercell and the surface area, respectively. The degree of relaxation (R) was calculated as $R = 100(\gamma_u - \gamma_r)/\gamma_u$.

The temperature-corrected energy $[E_M(T,p^\circ)]$ for the adsorbate molecule was calculated according to

$$E_M(T, p^\circ) = E_M - TS(T, p^\circ) \tag{3}$$

where E_M is the calculated DFT energy for the isolated adsorbate, T is the temperature, and $S(T,p^\circ)$ is the experimental entropy in the standard state, extracted from thermodynamic tables.[134] The average adsorption energy for the adsorbates $[E_{ads}(T,p^\circ)]$ was obtained via

$$E_{ads}(T, p^\circ) = \frac{E_c - (E_r + n_M E_M(T, p^\circ))}{n_M} \tag{4}$$

where E_c is the energy of the slab with the adsorbed species and n_M is the number of surface-bound adsorbates.

For the hydrogenated surfaces, the effect of temperature on the surface free energy $[\sigma(T,p)]$ was introduced as follows[109,115,135,136]

$$\sigma(T, p) = \gamma_r + C\left(E_{ads}(T, p^\circ) - RT \ln \frac{p_{H_2}}{p^\circ}\right) \tag{5}$$

where C is the coverage of hydrogen. The last term represents the change in free energy of the H_2 gas, assuming ideal gas behavior, at constant temperature when its partial pressure changes from p° to p_{H_2}.

The activation energy (E_{ai}) was calculated as the difference of the energy of the saddle point and the energy of the reactants, where the index i refers to each of the three elemental steps that we simulated. The energy of the elemental step (ΔE_i) was obtained as the difference of the energy of the products and the energy of the reactants.

3. RESULTS AND DISCUSSION

3.1. Bulk of β-Co Metal. β-Co metal has the face-centered cubic (fcc) structure characterized by the space group $Fm\bar{3}m$ (no. 225).[137] Figure 1a displays the conventional cubic unit cell containing four Co atoms and their periodic images. The metal lattice has a cubic close-packed (ccp) arrangement along the [111] direction, implying that the stacking sequence can be represented as *ABC* for the atomic planes perpendicularly intercepted, as shown in Figure 1b. Each metal atom has a coordination number of 12 equidistant nearest neighbors, which are distributed in the Wyckoff 4*a* positions with coordinates (0, 0, 0). Assuming that Co atoms are congruent spheres, the Co−Co interatomic distance (d) is related to the lattice parameter (a) as $d = a/\sqrt{2}$, ensuring a packing efficiency of 74.05%. As expected for the most dense known packing of the ccp metals, the empty space of the cell is composed of eight tetrahedral holes and four octahedral cavities. These voids are responsible for the adsorption and catalytic properties of Co once they are exposed at the surfaces, as discussed in Sections 3.3 to 3.4.

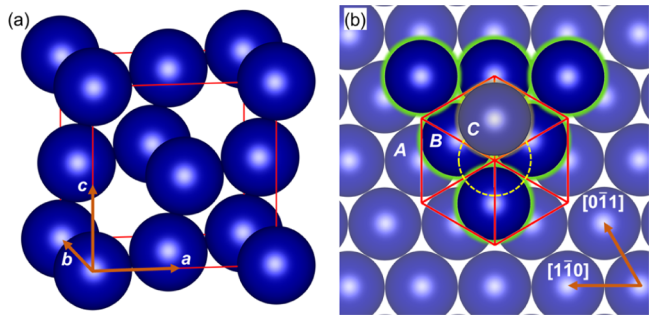

Figure 1. Schematic representation of (a) the face-centered cubic (fcc) conventional unit cell containing four Co atoms and (b) cubic close-packed (ccp) arrangement along the [111] direction. The atomic layers *A*, *B*, and *C* as well as the crystallographic directions are indicated. The atoms in the *B* (*C*) layer are highlighted in green (orange). The dashed yellow circle represents the position where one atom from the *A* layer would be stacked in a hexagonal close-packed (hcp) arrangement along the [111] direction.

The lattice parameter for the optimized cubic unit cell of Co bulk was calculated at a = 3.521 Å, which is marginally underestimated by 0.65% with respect to the value obtained from X-ray diffraction experiments.[138] Although the atoms were allowed to move freely during the lattice relaxation, we found that they prefer to remain at their ideal Wyckoff 4*a* crystallographic coordinates with the perfectly symmetric 12-

https://doi.org/10.1021/acs.jpcc.1c00254
J. Phys. Chem. C 2021, 125, 11891−11903

fold coordination. The cell shape was also fully optimized, but it stayed in the undistorted fcc geometry with an equilibrium volume of $\hat{V}$ = 10.913 Å^3 atom^{-1}. The magnetic moments (m_s) were integrated within the Bader atomic volumes, and we found that the value of m_s = 1.78 μ_B atom^{-1} simulated for Co is in excellent agreement with previous reports.[139−143] The decimal value of the magnetic moment obtained for Co is characteristic of metals and represents the balance of the number of electrons in the majority and minority spin channel.[144,145] Figure S1 (Supporting Information) displays a marked asymmetry for the Co 3*d* bands crossing the Fermi level in both channels of the spin of the polarized electronic density of states (DOS), which is typical of ferromagnetic materials.

3.2. Pristine Co(111) Surface. Next, we modeled the pristine planar termination of the low-Miller index (111) surface of Co, shown in Figure 2. The 9-fold metal atoms

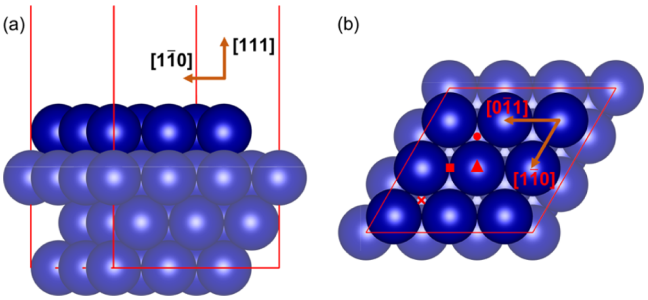

Figure 2. (a) Side and (b) top views of the Co(111) surface. Layers containing atoms with dangling bonds are highlighted. Crystallographic directions and the symmetrically inequivalent adsorption sites atop (▲), bridge (■), face-centered cubic (fcc, ×), and hexagonal close-packed (hcp, ●) are indicated.

exposed at the top surface layer have the two-dimensional hexagonal-packing arrangement typical of the close-packed structure, with three dangling bonds in the plane where the bulk was severed. The primitive unit of the (111) surface is a rhombus with a 2-fold rotational symmetry whose edges lie in the [0$\bar{1}$1] and [1$\bar{1}$0] directions, which periodic repetition creates the extended surface. The surface energy computed for the unrelaxed slab is γ_u = 195 meV Å^{-2}, which suffers only a minor degree of relaxation R = 0.59% during optimization. However, the surface energy calculated for our half-relaxed slab is just 7.7 meV Å^{-2} more stable than the value reported by Skriver and Rosengaard.[146] Figure 2a illustrates that this relaxation corresponds to 0.004 Å of vertical atomic displacement toward the bulk for the subsurface layer and to an outward migration of 0.047 Å for the layer containing the under-coordinated atoms with nil horizontal shifts. We found that the creation of the surface induces minor changes in the atomic charges (q), with the atoms in the subsurface layer loosing 0.019 e$^-$, whereas those in the surface layer gained 0.006 e$^-$. Our calculations suggest that the magnetic moment of the Co exposed at the surface is just 0.10 μ_B atom^{-1} larger than for the atoms in the bulk. However, the atoms in the subsurface layer did not experience any noticeable change of magnetization. We also calculated the work function at a value of 4.918 eV for the Co(111) surface, which compares well with previous works.[146,147] As our computational model captures the main structural, thermodynamic, magnetic, and electronic properties of the fcc Co(111) surface, we are confident that the DFT methods employed in this study are reasonably accurate.

3.3. Single-Molecule Adsorption on the Co(111) Surface. We have investigated the adsorption of the single syngas molecules H_2 and CO_2 on the Co(111) surface and their impact on the thermodynamic stability, the magnetic moments, charge transfers, and work function of the Co metal slab. We have also analyzed the structural properties of the adsorption configurations, the charge transfers between the molecules and the surface, as well as changes in the fundamental vibrational modes. Figure 2b displays the symmetrically inequivalent adsorption sites considered in this work, including (i) atop one Co, (ii) the bridge connecting two metal centres, and (iii) the fcc as well as (iv) the hcp trigonal holes formed between three atoms.

In order to assess the suitability of our computational methods to describe the structure and energies of the adsorbates, we have calculated their bond distances (d), dissociation energies (D), as well as their vibrational frequencies (ν) and compared them with experimental values, see Table 1. For the CO and H_2 molecules, we overestimated their bond distances by only 0.015 and 0.009 Å, respectively, with respect to the experimental values.[148] The dissociation energies for these diatomic molecules were calculated taking the ground state H [$1s^1$] as well as the triplet C [$1s^2 2s^2 2p^2$] and O [$1s^2 2s^2 2p^4$] atoms as reference. Our simulations predicted a slightly larger dissociation energy for CO in the order of ∼0.4 eV from the experimental D_{CO}, whereas for H_2, we found a much better agreement within ∼0.1 eV of the reported D_{H_2}.[149] The vibrational frequency is 2126 and 4334 cm^{-1} for the isolated CO and H_2, respectively, while the experimental values are red-shifted at 2143 and blue-shifted at 4161 cm^{-1} for the gas phase molecules, respectively.[148]

3.3.1. CO Interaction with the Co(111) Surface. A single CO molecule was incorporated in four different relative orientations to the symmetrically inequivalent positions considered, that is, perpendicular to the surface with either the (i) C or the (ii) O end interacting with a Co atom and parallel to the surface with the molecular C_n rotational axis aligned with (iii) the trigonal holes or the (iv) first-neighbor Co atoms. We initially placed the CO molecule at 2.0 Å from the surface and then carried out full geometry optimizations. Our simulations suggest that the CO molecule always adsorbs molecularly and perpendicularly through its C atom to the Co(111) surface. The adsorption energies for a single CO molecule binding to the Co(111) surface, which are listed in Table 2, show that these interactions are exothermic processes,

Table 1. Intramolecular Bond Distance (d), Dissociation Energy (D), and Vibrational Frequency (ν) Calculated for the Isolated CO and H_2 Molecules

	calculated			experimental		
molecule	d (Å)	D (eV)	ν (cm^{-1})	d (Å)[148]	D (eV)[149]	ν (cm^{-1})[148]
CO	1.143	11.502	2126	1.128	11.09 ± 0.02	2143
H_2	0.750	4.541	4334	0.741	4.447 ± < 0.001	4161

https://doi.org/10.1021/acs.jpcc.1c00254
J. Phys. Chem. C 2021, 125, 11891−11903

Table 2. Adsorption Energies (E_{ads}) at 0 K, Average Interatomic Distances (d), Wavenumbers for the Stretching Vibrational Modes (ν), and Charge Transfers (Δq) Calculated for a Single CO Molecule Interacting with the Four Symmetrically Inequivalent Adsorption Sites Considered for the Co(111) Surface[a]

position	E_{ads} (eV)	d_{Co-C} (Å)	d_{C-O} (Å)	ν_{C-O} (cm^{-1})	Δq (e^-)	Φ (eV)	σ (meV $Å^{-2}$)
atop	−3.847	1.7336	1.1710	1943	−0.2951	4.798	115
bridge	−3.884	1.9507	1.1856	1803	−0.4219	4.496	115
fcc	−3.952	1.9795	1.1962	1743	−0.4594	5.328	113
hcp	−3.931	2.0431	1.1870	1794	−0.4239	4.684	114

[a]The surface free energies (σ) at 0 K and work functions (Φ) are also reported. Negative values of Δq indicate charge transfer from the surface to the adsorbate.

releasing E_{ads} ∼−3.9 eV within a range of values of no more than 0.1 eV. The trend of the calculated adsorption energies of the CO molecule is in reasonable agreement with the coordination number of the binding sites. For example, the atop adsorption is the least favored interaction on thermodynamic grounds with E_{ads} = −3.847 eV, as the C atom can only coordinate one surface metal atom. For the bridge site, where the molecule moved slightly toward the hcp hole during optimization, the adsorption energy is only 0.037 eV more favorable than at the atop position, since the CO interacts with two surface Co atoms. The almost degenerate interactions at the hcp and the fcc hole positions result in the largest adsorption energies because the CO molecule can bind to three Co atoms, see Figure 3a. Note that we also tested the

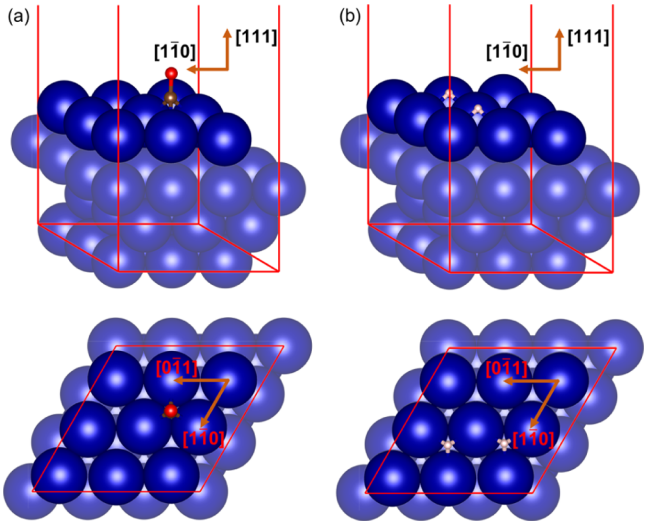

Figure 3. (a) Molecular adsorption of CO and (b) dissociative adsorption of H_2 on the face-centered cubic (fcc) and hexagonal close-packed (hcp) sites, respectively, of the Co(111) surface. Side (top panels) and top (bottom panels) views are displayed. Co atoms are in blue, C atoms are in brown, O atoms are in red, and H atoms are in white. Layers containing atoms with dangling bonds are highlighted. Crystallographic directions are indicated.

possible dissociative adsorption of the CO molecule, where the intramolecular triple bond is broken, but found it to be less favorable owing to its comparatively smaller adsorption energy of E_{ads} = −1.86 eV. The adsorption of CO has clearly affected several structural, vibrational, electronic, and thermodynamic properties of the surface, the molecule, and the interactions, as shown in Table 2. The simulated Co−C distances are inversely proportional to the coordination number of their adsorption sites, suggesting that the single bond formed in the atop position with d_{Co-C} = 1.7336 Å is stronger than any one of the three interactions at the trigonal holes. The overall strength of the interaction determines the C−O intramolecular distance, which has the largest value of d_{C-O} = 1.1962 Å for the most favorable adsorption on the fcc site. The elongation and therefore weakening of the C−O bond induces a red-shift in the stretching vibrational mode of the adsorbate with respect to the isolated molecule, with a smallest wavenumber of 1743 cm^{-1} calculated for the most stable adsorption mode on the fcc hole. The changes of the C−O intramolecular distance can be rationalized in terms of the charge transfer from the surface to the π^* antibonding molecular orbitals of the adsorbate. The CO molecule receives ∼−0.3 e^- in the atop position, approximately −0.42 e^- in both the bridge and hcp site and −0.46 e^- in the fcc hole, in agreement with the trend of adsorption energies. Interestingly, this charge transfer partially depletes the most loose electrons from the surface, resulting in a work function required to remove tighter bound electrons that is only larger at Φ_{fcc} = 5.328 eV for the adsorption at the fcc site than for the pristine surface. Finally, the adsorption of a single CO molecule increases the stability of the surface with respect to the pristine slab, as evidenced by the reduction of its surface free energy by around 80 meV $Å^{-2}$.

3.3.2. H_2 Interaction with the Co(111) Surface. We next investigated the interaction of a single H_2 molecule with the Co(111) surface, by placing the adsorbate in the same orientations and distance considered previously for CO, followed by a full geometry relaxation. Since the two H atoms are equivalent, we only needed to explore one of the perpendicular orientations of the molecule with respect to the surface. We do not describe the adsorption of H_2 onto the bridge position, as we did not find evidence of this coordination configuration after optimization. Table 3 summarizes the calculated adsorption energies for H_2, which although negative, are generally less favorable than those for the interaction of CO with the same positions of the Co(111) surface. We observe that the adsorption energies for H_2 are more dispersed than for CO, as the only molecular interaction to the atop position releases 1.129 eV less than the dissociated configuration on the vicinal hcp and hcp site with the largest binding energy. Furthermore, the type of vicinal trigonal holes involved in the interactions with the dissociated H atoms plays a key role in their adsorption energies, which order of increasing stability is E_{ads}(fcc, hcp) > E_{ads}(fcc, fcc) > E_{ads}(hcp, hcp) varying by approximately 0.17 eV. As a result of the short H radius, the average binding distance to the surface is clearly smaller than for CO. However, the H atoms prefer to sit ∼0.15 Å closer to the surface in the atop position, where only one Co atom is coordinated, than at the vicinal hcp cavity, where three metal atoms are involved. The H atoms interact approximately 0.02 Å further away with the vicinal fcc, fcc, and fcc, hcp sites than with the hcp and hcp holes, in agreement with their

https://doi.org/10.1021/acs.jpcc.1c00254
J. Phys. Chem. C 2021, 125, 11891−11903

Table 3. Adsorption Energies (E_{ads}) at 0 K, Average Interatomic Distances (d), and Charge Transfers (Δq) Calculated for a Single Dissociated and Molecular H_2 Interacting with the Symmetrically Inequivalent Adsorption Sites Considered for the Co(111) Surface[a]

adsorbate	position	E_{ads} (eV)	d_{Co-H} (Å)	d_{H-H} (Å)	Δq (e^-)	Φ (eV)	σ (eV Å^{-2})
H_2	atop	−2.311	1.6072	0.9045	−0.0780	4.356	147.2
2H	fcc, fcc	−3.251	1.7725	2.7353	−0.6100	4.367	127.7
2H	fcc, hcp	−3.098	1.7710	1.9907	−0.5747	4.704	130.9
2H	hcp, hcp	−3.440	1.7573	2.5193	−0.6087	4.506	123.8

[a]The surface free energies (σ) at 0 K and work functions (Φ) are also reported. Negative values of Δq indicate charge transfer from the surface to the adsorbate.

different adsorption energies, see Figure 3b. The intramolecular H−H distance d_{H-H} stretched by only 0.16 Å with respect to the isolated H_2 confirms that the adsorbate only remains in the molecular form when it interacts with the atop position, whereas it dissociates spontaneously at the other adsorption sites on the Co(111) surface. The H−H distance is between 0.5 and 0.7 Å larger for the vicinal fcc, fcc and hcp, hcp sites that for the fcc and hcp cavities, which can be rationalized based on their different geometric relationship with the radius of the metal cobalt atom (r_{Co}) and their atomic charges. For instance, both the vicinal fcc, fcc, and hcp, hcp sites are separated by $2r_{Co}$ cos 30° = 2.1562 Å, whereas the distance between the vicinal fcc and hcp holes is $2r_{Co}$ cos 60° = 1.2449 Å. The charge transfers confirm that the H atoms become negatively charged once they attach to the surface but less than compared to the CO molecule. The molecularly adsorbed H_2 receives just −0.0780 e^- at the atop position, which is insufficient to break the intramolecular bond, while charge transfers larger than −0.5 e^- lead to dissociation and Coulomb repulsion between the H atoms. Our computed Bader charges suggest that charge donation is at least 0.04 e^- larger in the fcc, fcc and hcp, and hcp sites than in the fcc and hcp holes. The pattern of a smaller work function suggests that the Co(111) surface becomes more catalytically reactive after adsorbing a single H_2 molecule in any of the geometries considered. As expected, the surface free energies indicate that the material gains stability upon adsorption of H_2.

3.4. FT Processes. We propose three main mechanisms to model the FT processes on the Co(111) surface. The modeled pathways cover the catalytic conversion of H_2 and CO into important intermediates, which in turn lead to the target hydrocarbon C_2H_6 and byproduct H_2O, as well as the unwanted CH_4 and CO_2. Our choice of possible pathways will allow us to assess their different feasibilities and compare them with experiments. For the construction of the energy diagrams, we have chosen the most favorable adsorption configuration for the reactants, intermediates, and final products, which were linked by saddle points and MEPs.

3.4.1. Hydrogenolysis of CO. Figure 4 shows the MEP for the coadsorption of CO and H, followed by the catalytic conversion into a number of intermediates on the Co(111) surface. The cNEB method employed for the simulation of the MEP has been used in previous works, offering saddle point energies and structures in close agreement with experiment.[150−152] Since we are interested in the reaction between CO and H, we decided to place these species in the closest and most stable fcc and hcp binding sites, respectively. We found that the coadsorption is a very favorable process, releasing a binding energy of E_{ads} = −4.70 eV, which is, however, 972 meV smaller than for the infinitely separated species discussed in Section 3.3. Once coadsorbed, both the CO and H species

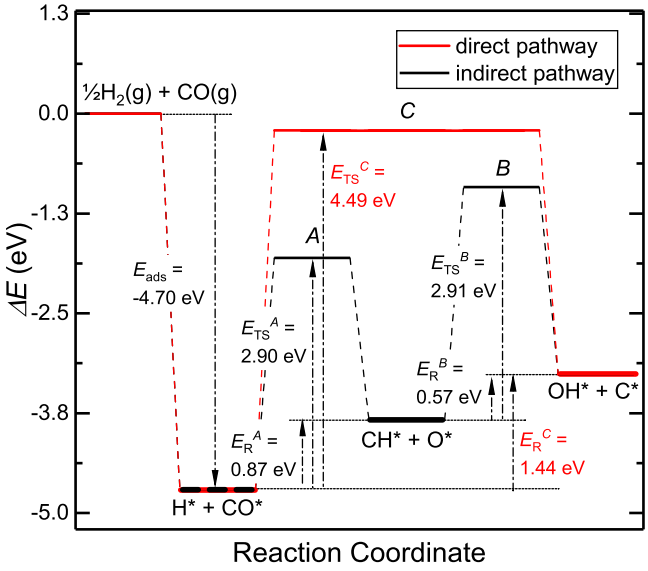

Figure 4. MEPs for the CO reduction by H on the Co(111) surface. Minimum states are denoted by bold lines and saddle points are denoted by narrow lines linked by dashed lines. Energies are referenced to the isolated 1/2H_2(g) + CO(g) molecules. Adsorbed species are denoted using the symbol *.

remain in their initial adsorption sites but marginally further away from the surface by 0.009 Å and closer to it by 0.004 Å, respectively, than during the single molecule adsorption. The charge analysis of this state indicates that both the H and CO become slightly less negative by 0.0188 and 0.0093 e^- than after the single molecule adsorption, as they share two of the three surface Co atoms they coordinate. The catalyst surface in this reaction state can be characterized using STM imaging, illustrating the distribution of intermediates. Figure 5 was constructed using a sample bias of V = −2.5 eV, which is the lower limit used for the integration of the partial charge density of the surface up to the Fermi level (E_F) upper boundary. These images depict the three-dimensional distribution of the occupied states in the vicinity of the Fermi level, which is equivalent to the tunneling of the electrons from the surface to the tip of the STM probe. Figure 5a is the control STM image for the pristine surface, which was acquired at an electron density (ρ) of 0.3177 eÅ^{-3} and at a distance (d) of 0.89 Å to the tip, illustrating the ccp stacking of Co atoms along the [111] direction. The exposed Co atoms in the surface layer are depicted brighter than those fully coordinated in the subsurface, and each atomic plane has the hexagonal packing characteristic of the β-Co metal. Figure 5b represents the state where the CO and H species are coadsorbed on the Co(111) surface. This STM image, which was obtained with a distance

https://doi.org/10.1021/acs.jpcc.1c00254
J. Phys. Chem. C 2021, 125, 11891−11903

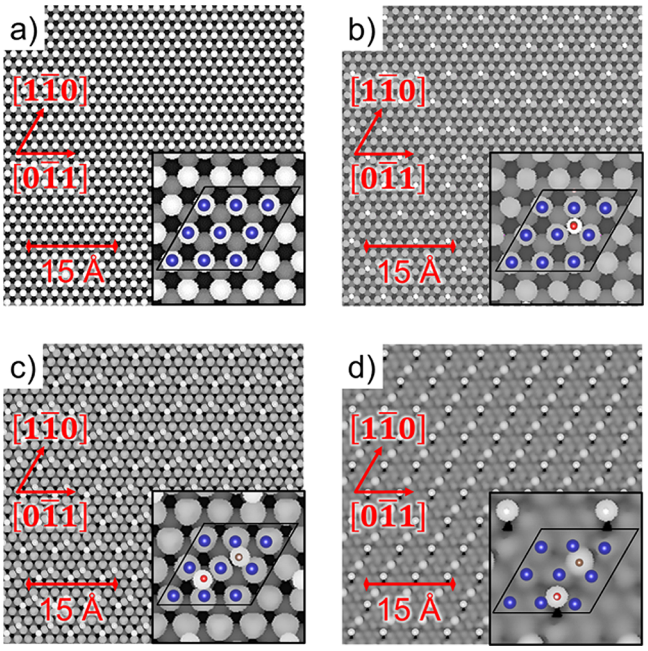

Figure 5. Simulated STM images of (a) pristine Co(111) surface and following the coadsorption of (b) H and CO, (c) CH and O, and (d) OH and C. The STM images were generated using a bias of $V = -2.5$ eV, electron densities of (a) $\rho = 0.3177$ eÅ^{-3}, (b) $\rho = 0.25142$ eÅ^{-3}, (c) $\rho = 0.1213$ eÅ^{-3}, and (d) $\rho = 0.0512$ eÅ^{-3} as well as a tip distance of (a) $d = 0.89$ Å, (b) $d = 0.28$ Å, (c) $d = 0.12$ Å, and (d) $d = 0.15$ Å. Inset shows enlargement of the STM image for the surface unit cell. Co atoms are in blue, C atoms are in brown, O atoms are in red, and H atoms are in white. Crystallographic directions are indicated.

of 0.28 Å to the tip and at a density of 0.25142 eÅ^{-3}, clearly shows the protruding CO molecule perpendicularly adsorbed on the fcc hole. However, our simulated image is unable to resolve the small H atom, as its electronic density cannot interact with the hypothetical STM tip.

The indirect pathway leads our system to the formation of the CH intermediate. In a concerted step, the H atom migrates to the side of the CO molecule, which loses its O atom. The formed CH species remains in the cavity previously filled by the reactant CO, while the O atom moves to a nearby hcp site, where it may undergo further reduction. This is an endothermic process with a reaction enthalpy of $E_RA = 0.87$ eV and an activation energy of $E_{TS}A = 2.90$ eV. Following this substitution reaction, the O atom attaches to the surface at 1.88 Å, whereas the reduced C atom moves 0.24 Å closer to the surface. The STM image for the reaction step where CH and O are coadsorbed on the Co(111) surface was simulated using an electron density of 0.1213 eÅ^{-3} and a distance of 0.12 Å to the tip, as shown in Figure 5c. The adsorbates are well defined, especially the O atom in the hcp cavity, which is displayed slightly brighter than the CH species in the fcc site.

The final step in the mechanism is the generation of OH and C, following both the direct and indirect pathways. In the resulting structure, the C remains attached to the fcc cavity, but the H atom is transferred 1.4 Å from the CH species to the O atom, which is pulled to a nearby fcc site. The OH group is adsorbed to the trigonal hole at an angle of approximately 110° with respect to the surface. Figure 5d illustrates the STM image for the reaction step where CH and O are coadsorbed on the Co(111) surface, which was produced at a distance of 0.15 Å to the highest atom and an electron density of 0.0512 eÅ^{-3}. Similar to the previous reaction step, the intermediates are well defined in the image. Interestingly, we noticed that the contrast between the Co atoms of the top surface and subsurface layers becomes weaker during the reaction, indicating the presence of adsorbates on the surface. The conversion of CH and O into OH and C is endothermic by 0.57 eV, and its activation energy is essentially the same that was calculated for the saddle point *A*. The alternative direct pathway requires crossing the saddle point *C*, which has an energy just 0.21 eV smaller than the adsorption energy released by the syngas mixture. In summary, the coadsorption of CO and H provides enough energy for the system to surmount the saddle point with even the largest energy, which suggests that at the high temperatures typical of the FT process, all species reported in Figure 4 are accessible, coexist, and are in equilibrium. We did not consider intermediate triatomic species such as COH*, CHO*, or the tetratomic CHOH*

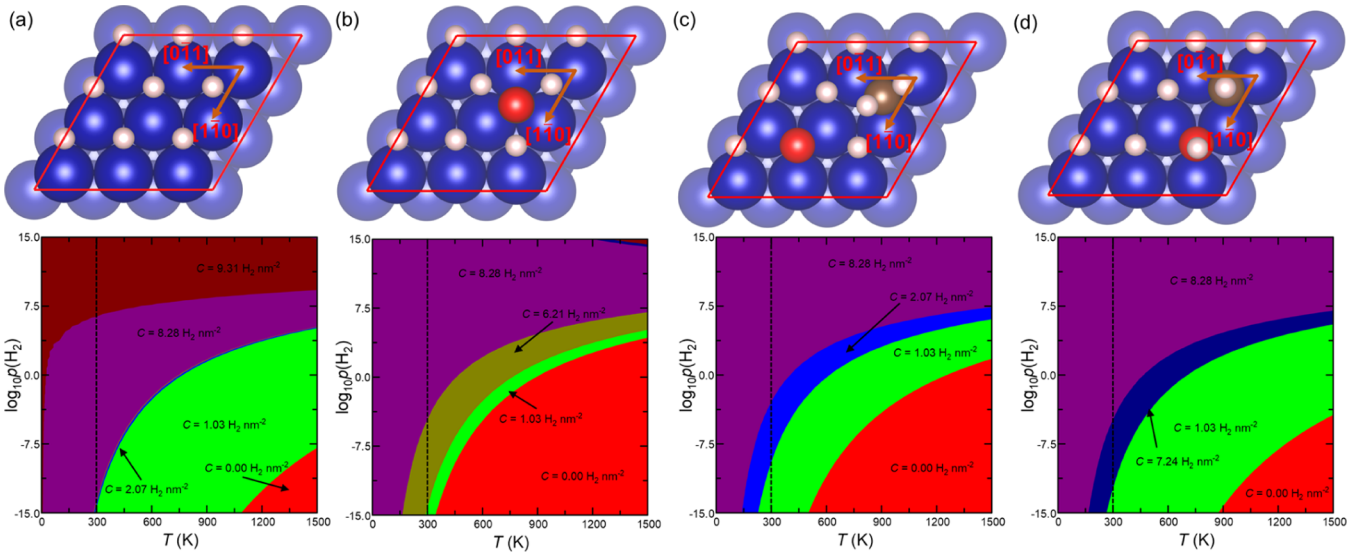

Figure 6. Phase diagrams for the (a) pristine Co(111) surface as well as for the surfaces containing (b) 2.07 CO nm^{-2}, (c) 2.07 CH nm^{-2}, and 2.07 O nm^{-2}, and (d) 2.07 OH nm^{-2} and 2.07 C nm^{-2} as functions of partial pressure of H_2 and temperature.

https://doi.org/10.1021/acs.jpcc.1c00254
J. Phys. Chem. C 2021, 125, 11891−11903

adduct for the sake of simplicity. The resulting number of possible intermediates and saddle points can be very large, making the MEP and simulations complicated and difficult to rationalize.

3.4.2. Effect of H Coverage. We have evaluated the relative stability of the Co(111) surface containing the intermediate species discussed in Section 3.4.1 as a function of the partial pressure of H_2, as we are interested in assessing the ratio of their equilibrium coverages under the FT conditions. This approach has been used previously, providing results in excellent agreement with experiments.[109,115,136] Figure 6 displays the H_2 pressures as a function of the desorption temperatures for the pristine Co(111) surface as well as containing a single CO molecule, the coadsorbed CH and O species, and the coadsorbed OH and C intermediates, as calculated according to eq 5. We have simulated different coverages of H, by creating up to a full monolayer of this atom in the most stable hcp cavity found for the single atom. Thus, our choice of supercell size allows the addition of up to nine H atoms to the Co(111) surface, shown in Figure 6a. For a H_2-rich syngas mixture in equilibrium with the catalyst, we can still ensure that surface-bound CO is available, as the species prefer different types of adsorption sites, and CO replaces H under conditions of competitive adsorption, see Figure 6b. The very reactive C and CH intermediates become easily protonated, as the surface H coverage is increased, as displayed in Figure 6c,d.

Figure 6a shows that the pristine Co(111) surface requires temperatures above 1200 K and pressures below $10^{-7.5}$ bar of H_2 to remain free of H atoms. A coverage of 1.03 H_2 nm^{-2}, that is, one H atom in our surface, becomes stable between the maximum pressure of 10^4 bar of H_2 and the minimum temperature of 300 K. A larger coverage of 2.07 H_2 nm^{-2}, for the surface containing two H atoms, has a very narrow range of stability adjacent to the border of the 1.03 H_2 nm^{-2} coverage. The surface is able to accommodate eight H atoms if the pressure of H_2 is increased up to 10^8 bar for temperatures larger than 300 K, whereas this coverage of 8.28 H_2 nm^{-2} remains the preferred one below pressures of 1 bar of H_2 at 30 K. The full monolayer of H with a coverage of 9.31 H_2 nm^{-2} is achieved at pressures of H_2 larger than those required for the surface containing eight H atoms.

We found that the interaction of the surface with H_2 is affected differently depending on the coadsorbed species. For example, the coadsorption of CO reduces the range of temperatures required for H to bind with respect to the pristine surface, indicating that a low temperature hydrogenation is the most favorable scenario, see Figure 6b. For the system containing the CO species, we can see that the surface does not contain H atoms above ~1150 K at 10 bar of H_2 pressure, which is typical of the FT process. As the temperature is reduced, the surface is able to bind 1.03 H_2 nm^{-2}, equivalent to one H atom in our supercell. Temperatures below 900 K allow the adsorption of six H atoms, corresponding to a coverage of 6.21 H_2 nm^{-2}. The most dense coverage of 8.28 H_2 nm^{-2} is then achieved between 0 and 550 K, indicating that at room temperature, the Co(111) surface will be fully covered by H atoms.

Compared to CO, CH increases the stability of high coverages of H at the surface, which enables the coadsorption of both species at lower temperatures. In general, the pattern of the surface phase diagram for the surface containing a single CH species is very similar to the system with a surface-bound CO molecule, although more intermediate coverages of H_2 are permitted when CH is coadsorbed. For the catalyst containing either CH or CO, our calculated phase diagrams provide evidence that the Co(111) surface is likely to have a coverage between 6.21 and 8.28 H_2 nm^{-2} under the experimental conditions of the FT process, that is, 10−60 bar and 473−573 K. This H coverage, which is equivalent to 6−8 H atoms adsorbed in our surface supercell, indicates that the ratio of equilibrium coverages (C) is $C_H/C_{CO,CH,OH}$ > 6:1 at the temperature conditions required for the FT process. This analysis is in excellent agreement with experiment, as it is well known that an excess of H_2 with respect to CO is needed for the formation of alkanes with the general formula C_nH_{2n+2}.

3.4.3. Formation of C_2H_6. From the phase diagram derived in Section 3.4.2, we know that large coverages of H can coexist with a number of C1 intermediates on the Co(111) surface and therefore C_C/C_H = 1:3 is a sensible ratio of equilibrium coverages to consider as the starting configuration for the formation of hydrocarbons on the Co(111) surface. These conditions lead us to three possibilities, shown in Figure 7,

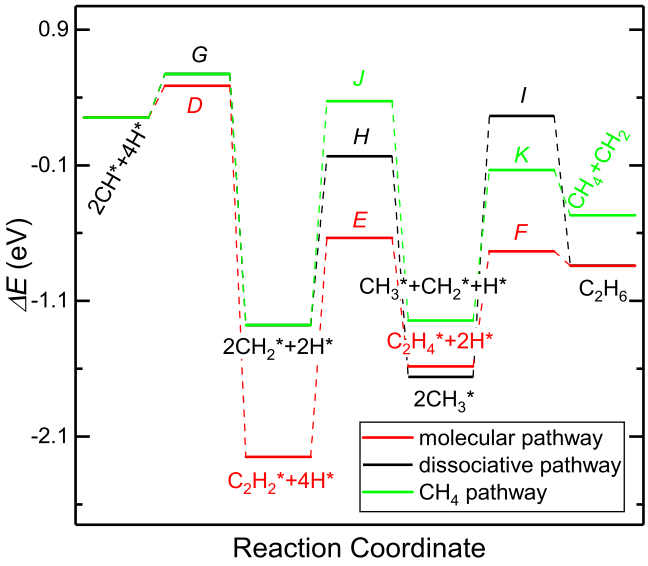

Figure 7. MEPs for the formation of C_2H_6 and CH_4 on the Co(111) surface. Minimum states are denoted by bold lines and saddle points are denoted by narrow lines linked by dashed lines. Energies are referenced to the adsorbed species 2CH* + 4H*.

which comprise the molecular and dissociated pathways for the formation of C_2H_6 as well as the conversion of the CH intermediate into the unwanted CH_4. In the molecular pathway, two CH* species react to form a surface-bound acetylene (C_2H_2*) molecule, which is 2.2 eV lower in energy than the initial state, after overcoming a small barrier of 0.5 eV, which corroborates the thermodynamic and kinetic feasibility of the formation of the C−C bond. As a result of this reaction, one of the C atoms leave its fcc site to occupy a neighboring hcp surface hole, closer to the C atom that remained in its catalytic site. The acetylene molecule does not lie linearly along the surface as the C atoms display a pseudo sp^2 trigonal geometry, where the two H atoms are pointing outward. As a result, the C atoms of the C_2H_2* intermediate move away from the surface by 0.2 Å. Given the large number of H atoms adsorbed on the surface, the C_2H_2* molecule is able to undergo further reduction. The addition of two H atoms transforms the intermediate into the olefin molecule ethene

https://doi.org/10.1021/acs.jpcc.1c00254
J. Phys. Chem. C 2021, 125, 11891−11903

(C_2H_4*) in an endothermic process with a reaction energy of 0.6 eV, which requires 1.6 eV to cross the saddle point in the MEP. The hydrocarbon molecule moves further away from the surface of the catalyst and coordinates the Co atoms using large pseudo-hybrid sp^3 tetrahedral orbitals. In the last elemental step of this pathway, the hydrocarbon intermediate becomes saturated and physisorbed to the surface, with the closest C remaining at a distance of 3.13 Å from the closest Co atom. Although this process is endothermic by ∼1.0 eV, the transition state barrier has a modest energy of 1.2 eV.

In the alternative dissociated pathway, we first simulated the hydrogenation of the C1 species and finally the coupling of the C atoms, as shown in Figure 7. Our calculations suggest that the intermediates of the dissociated pathway are less stable than in the molecular pathway, while the saddle points are of higher energy. For example, the dissociated surface species $2CH_2$* + 2H* are ∼1 eV higher in energy than the molecular intermediate C_2H_2* + 4H*. Moreover, the transition states *G*, *H*, and *I* for the dissociated pathway lie above their counterparts *D*, *E*, and *F* in the molecular pathway, suggesting that the formation of C_2H_6* proceeds via the addition of CH species to the reaction intermediate. Finally, we also tested the formation of CH_4*, which is an unwanted product in the FT reaction. However, the intermediates and transition states are the least stable in the energy diagram displayed in Figure 7, which explains the lack of selectivity by Co for the formation of the smallest molecular weight hydrocarbon. Note that testing the selectivity toward hydrocarbons containing more than five carbon atoms would entail modeling at least 5 CH groups coadsorbed with 7 H atoms, which is beyond the size constrains allowed by our cobalt Co(111) surface model. Moreover, simulating the formation of alkanes longer than propane is a formidable computational task, as the number of structural isomers that has to be considered increases significantly with the number of C atoms. However, based on the relative energies of the intermediates and saddle points presented in Figure 7, we speculate that a continuous supply of syngas will favor the growth of the hydrocarbon chain over the hydrogenation of the C1 and C2 species.

4. CONCLUSIONS

We have employed DFT calculations to simulate the conversion of a mixture of H_2 and CO (syngas) into hydrocarbons on the planar bulk-like Co(111) surface. We have elucidated the structures and energies of the single molecule adsorption for the reactants and demonstrated their role in the changes observed in the interatomic distances, the wavenumbers of the fundamental vibrational modes, charge transfers, surface free energies, and work functions. We found that CO binds molecularly the catalyst surface, whereas H_2 dissociates upon adsorption. Both syngas species bind preferentially to different types of trigonal holes on the Co(111) surface.

Although still highly exothermic, the vicinal-site coadsorption of single CO and H species in close proximity is a process, which is approximately 1 eV less favorable than the adsorption of the infinitely separated adsorbates. The MEP calculated for the hydrogenolysis of the CO molecule suggests that the energy released during coadsorption is enough for the system to cross the saddle points and form important intermediates such as CH, OH, and O. We successfully simulated the phase diagrams for the surface containing a single intermediate molecule as a function of the partial pressure of hydrogen and temperature. The (111) surface of the catalyst is further stabilized when the ratio of coverages (*C*) is $C_H/C_{CO,CH,OH}$ > 6:1 at the temperature conditions required for the FT process, which explains the excess of H species required for the formation of hydrocarbons.

The surface-bound intermediates are slightly less stable than the syngas molecules, but the simulated energy diagrams show that they can react to form hydrocarbons. The reaction profiles suggest that the Co(111) surface has the largest selectivity toward C_2H_6, which is our model of a straight-chain alkane. The most favorable mechanistic pathway was calculated when two CH species form an adsorbed acetylene (C_2H_2) molecule that then undergoes hydrogenation until the hydrocarbon is fully saturated. The generation of CH_4 or the coupling of two methyl (CH_3) groups to create the C−C bond leads to unstable intermediates and high energy saddle points. The simulated STM images and wavenumbers for the fundamental vibrational modes are presented as a means to characterize the reaction coordinate for each pathway. These results allow direct comparison with experiments and explain the surface chemistry during the FT process.

Future work will involve microkinetic simulations to understand how the FT process takes place at different catalytic sites. The kinetic model for the conversion of CO and H_2 into hydrocarbons will allow us to predict the convex hull of the ground states. Most importantly, we will be able to carry out dynamic simulations at a range of conditions to calculate the turnover frequencies and compare them with experiments.

■ ASSOCIATED CONTENT

Supporting Information

The Supporting Information is available free of charge at https://pubs.acs.org/doi/10.1021/acs.jpcc.1c00254.

DOSs of the bulk Co (PDF)

■ AUTHOR INFORMATION

Corresponding Authors

David Santos-Carballal − *School of Chemistry, University of Leeds, Leeds LS2 9JT, U.K.; School of Chemistry, Cardiff University, Cardiff CF10 3AT, U.K.;* orcid.org/0000-0002-3199-9588; Email: D.Santos-Carballal@leeds.ac.uk

Nora H. de Leeuw − *School of Chemistry, University of Leeds, Leeds LS2 9JT, U.K.; Department of Earth Sciences, Utrecht University, Utrecht 3584 CD, The Netherlands*; Phone: +44 (0) 11 3343 9008; Email: N.H.deLeeuw@leeds.ac.uk, N.H.deLeeuw@uu.nl

Author

Abdelaziz Cadi-Essadek − *School of Chemistry, Cardiff University, Cardiff CF10 3AT, U.K.;* orcid.org/0000-0002-7754-735X

Complete contact information is available at: https://pubs.acs.org/10.1021/acs.jpcc.1c00254

Notes

The authors declare no competing financial interest.

■ ACKNOWLEDGMENTS

We acknowledge the Engineering and Physical Sciences Research Council (EPSRC grant EP/K009567) for funding. Via our membership of the UK's HEC Materials Chemistry Consortium, which is funded by EPSRC (EP/L000202/1 and

EP/R029431/1), this work used the ARCHER UK National Supercomputing Service (http://www.archer.ac.uk). This work was performed using the computational facilities of the Advanced Research Computing @ Cardiff (ARCCA) Division, Cardiff University. We also acknowledge the use of HPC Wales, Supercomputing Wales, and associated support services in the completion of this work. All data are provided in full in the Results and Discussion section of this paper.

REFERENCES

(1) Dry, M. E. The Fischer-Tropsch Process: 1950-2000. *Catal. Today* **2002**, *71*, 227−241.
(2) Dry, M. E. The Fischer-Tropsch (FT) Synthesis Processes. *Handbook of Heterogeneous Catalysis*; Wiley-VCH Verlag GmbH & Co. KGaA: Weinheim, Germany, 2008.
(3) Fischer, F.; Tropsch, H. Vergleichende Untersuchungen Über Lignin Und Cellulose. *Ber. Dtsch. Chem. Ges.* **1923**, *56*, 2418−2428.
(4) Fischer, F.; Tropsch, H. Über einige Eigenschaften der aus Kohlenoxyd bei gewöhnlichem Druck hergestellten synthetischen Erdöl-Kohlenwasserstoffe. *Ber. Dtsch. Chem. Ges.* **1926**, *59*, 923−925.
(5) de Klerk, A. *Fischer-Tropsch Refining*; Wiley-VCH Verlag GmbH & Co. KGaA: Weinheim, Germany, 2011.
(6) de Klerk, A. Fischer-Tropsch Process. *Kirk−Othmer Encyclopedia of Chemical Technology*; John Wiley & Sons, Inc.: Hoboken, NJ, USA, 2013.
(7) de Klerk, A.; Furimsky, E. *Catalysis in the Refining of Fischer-Tropsch Syncrude*; Royal Society of Chemistry: Cambridge, 2010.
(8) List, B. Catalytic Processes that Changed the World: 100 Years Max-Planck-Institut für Kohlenforschung. *Angew. Chem., Int. Ed.* **2014**, *53*, 8528−8530.
(9) King, D. L.; de Klerk, A. *Overview of Feed-to-Liquid (XTL) Conversion*; ACS Symposium Series; American Chemical Society, 2011; pp 1−24.
(10) Meyers, R. A. *Handbook of Synfuels Technology*; McGraw-Hill, 1984.
(11) Probstein, R. F. *Synthetic Fuels*; Dover Publications, 2013.
(12) Iglesia, E.; Soled, S. L.; Fiato, R. A. Fischer-Tropsch Synthesis on Cobalt and Ruthenium. Metal Dispersion and Support Effects on Reaction Rate and Selectivity. *J. Catal.* **1992**, *137*, 212−224.
(13) Soled, S. L.; Iglesia, E.; Miseo, S.; DeRites, B. A.; Fiato, R. A. Selective Synthesis of α-Olefins on Fe-Zn Fischer-Tropsch Catalysts. *Top. Catal.* **1995**, *2*, 193−205.
(14) Hibbitts, D. D.; Loveless, B. T.; Neurock, M.; Iglesia, E. Mechanistic Role of Water on the Rate and Selectivity of Fischer-Tropsch Synthesis on Ruthenium Catalysts. *Angew. Chem., Int. Ed.* **2013**, *52*, 12273−12278.
(15) Iglesia, E. Design, Synthesis, and Use of Cobalt-Based Fischer-Tropsch Synthesis Catalysts. *Appl. Catal., A* **1997**, *161*, 59−78.
(16) Li, S.; Krishnamoorthy, S.; Li, A.; Meitzner, G. D.; Iglesia, E. Promoted Iron-Based Catalysts for the Fischer−Tropsch Synthesis: Design, Synthesis, Site Densities, and Catalytic Properties. *J. Catal.* **2002**, *206*, 202−217.
(17) Baliban, R. C.; Elia, J. A.; Weekman, V.; Floudas, C. A. Process Synthesis of Hybrid Coal, Biomass, and Natural Gas to Liquids via Fischer-Tropsch Synthesis, ZSM-5 Catalytic Conversion, Methanol Synthesis, Methanol-to-Gasoline, and Methanol-to-Olefins/Distillate Technologies. *Comput. Chem. Eng.* **2012**, *47*, 29−56.
(18) Liu, G.; Larson, E. D.; Williams, R. H.; Kreutz, T. G.; Guo, X. Making Fischer-Tropsch Fuels and Electricity from Coal and Biomass: Performance and Cost Analysis. *Energy Fuels* **2011**, *25*, 415−437.
(19) Kreutz, T. G.; Larson, E. D.; Liu, G.; Williams, R. H. *Fischer−Tropsch Fuels from Coal and Biomass*; Princeton University, December 1, 2008.
(20) Steynberg, A. P.; Nel, H. G. Clean Coal Conversion Options Using Fischer-Tropsch Technology. *Fuel* **2004**, *83*, 765−770.
(21) Tijmensen, M.; Faaij, A. P. C.; Hamelinck, C. N.; Van Hardeveld, M. R. M. Exploration of the Possibilities for Production of Fischer Tropsch Liquids and Power via Biomass Gasification. *Biomass Bioenergy* **2002**, *23*, 129−152.
(22) van Steen, E.; Claeys, M. Fischer-Tropsch Catalysts for the Biomass-to-Liquid Process. *Chem. Eng. Technol.* **2008**, *31*, 655−666.
(23) Kim, Y. H.; Jun, K.-W.; Joo, H.; Han, C.; Song, I. K. A Simulation Study on Gas-to-Liquid (Natural Gas to Fischer-Tropsch Synthetic Fuel) Process Optimization. *Chem. Eng. J.* **2009**, *155*, 427−432.
(24) Vosloo, A. C. Fischer Tropsch: A Futuristic View. *Fuel Process. Technol.* **2001**, *71*, 149.
(25) Kamara, B. I.; Coetzee, J. Overview of High-Temperature Fischer-Tropsch Gasoline and Diesel Quality. *Energy Fuels* **2009**, *23*, 2242−2247.
(26) Ershov, M.; Potanin, D.; Gueseva, A.; Abdellatief, T. M. M.; Kapustin, V. Novel Strategy to Develop the Technology of High-Octane Alternative Fuel Based on Low-Octane Gasoline Fischer-Tropsch Process. *Fuel* **2020**, *261*, 116330.
(27) De Klerk, A. Can Fischer-Tropsch Syncrude Be Refined to on-Specification Diesel Fuel? *Energy Fuels* **2009**, *23*, 4593−4604.
(28) Muzzell, P. A.; Freerks, R. L.; Baltrus, J. P.; Link, D. D. Composition of Syntroleum S-5 and Conformance to JP-5 Specification. *Prepr.—Am. Chem. Soc., Div. Pet. Chem.* **2004**, *49*, 411−412.
(29) Freerks, R. L.; Muzzell, P. A. Production and Characterization of Synthetic Jet Fuel Produced from Fischer-Tropsch Hydrocarbons. *Prepr.—Am. Chem. Soc., Div. Pet. Chem.* **2004**, *49*, 407−410.
(30) Corporan, E.; DeWitt, M. J.; Belovich, V.; Pawlik, R.; Lynch, A. C.; Gord, J. R.; Meyer, T. R. Emissions Characteristics of a Turbine Engine and Research Combustor Burning a Fischer-Tropsch Jet Fuel. *Energy Fuels* **2007**, *21*, 2615−2626.
(31) Drozd, G. T.; Miracolo, M. A.; Presto, A. A.; Lipsky, E. M.; Riemer, D. D.; Corporan, E.; Robinson, A. L. Particulate Matter and Organic Vapor Emissions from a Helicopter Engine Operating on Petroleum and Fischer-Tropsch Fuels. *Energy Fuels* **2012**, *26*, 4756−4766.
(32) Timko, M. T.; Yu, Z.; Onasch, T. B.; Wong, H.-W.; Miake-Lye, R. C.; Beyersdorf, A. J.; Anderson, B. E.; Thornhill, K. L.; Winstead, E. L.; Corporan, E.; et al. Particulate Emissions of Gas Turbine Engine Combustion of a Fischer-Tropsch Synthetic Fuel. *Energy Fuels* **2010**, *24*, 5883−5896.
(33) Kinsey, J. S.; Squier, W.; Timko, M.; Dong, Y.; Logan, R. Characterization of the Fine Particle Emissions from the Use of Two Fischer-Tropsch Fuels in a CFM56-2C1 Commercial Aircraft Engine. *Energy Fuels* **2019**, *33*, 8821−8834.
(34) Kyoto Protocol To the United Nations Framework Convention on Climate Change; *United Nations Framework Convention on Climate Change (UNFCCC)—Conference of the Parties (COP): Kyoto*, 1997; p 21.
(35) Adoption of the Paris Agreement; *United Nations Framework Convention on Climate Change (UNFCCC)—Conference of the Parties (COP): Paris*, 2015; p 32.
(36) *Climate Change Act 2008 (c. 27)*. [Online]. London: The Stationery Office.; Available from: https://www.legislation.gov.uk/ukpga/2008/27, 2008.
(37) *The Climate Change Act 2008 (2050 Target Amendment) Order 2019*. SI 2019/1056. [Online]. London: The Stationery Office.; Available from: http://www.legislation.gov.uk/id/ukdsi/2019/9780111187654, 2019.
(38) Schulz, H. Short History and Present Trends of Fischer-Tropsch Synthesis. *Appl. Catal., A* **1999**, *186*, 3−12.
(39) Biloen, P.; Sachtler, W. M. H. Mechanism of Hydrocarbon Synthesis over Fischer-Tropsch Catalysts. *Adv. Catal.* **1981**, *30*, 165−216.
(40) Bell, A. T. Catalytic Synthesis of Hydrocarbons over Group VIII Metals. A Discussion of the Reaction Mechanism. *Catal. Rev.* **1981**, *23*, 203−232.
(41) Elstner, M.; Rao, B. R.; Schulz, H. No(14)C-Studien Zum Reaktionsmechanismus Der Fischer-Tropsch-Synthese. *Erdöl Kohle* **1970**, *23*, 651−655.

https://doi.org/10.1021/acs.jpcc.1c00254
J. Phys. Chem. C 2021, 125, 11891−11903

(42) Schulz, H.; Achtsnit, H. D. Olefin Reactions During the Fischer- Tropsch-Synthesis. *Rev. Port. Quim.* **1977**, *19*, 317−322.
(43) Schulz, H.; Erich, E.; Gorre, H.; van Steen, E. Regularities of Selectivity as a Key for Discriminating FT-Surface Reactions and Formation of the Dynamic System. *Catal. Lett.* **1990**, *7*, 157−167.
(44) Kummer, J. T.; Emmett, P. H. Fischer—Tropsch Synthesis Mechanism Studies. The Addition of Radioactive Alcohols to the Synthesis Gas. *J. Am. Chem. Soc.* **1953**, *75*, 5177−5183.
(45) Pichler, H.; Schulz, H. Neuere Erkenntnisse Auf Dem Gebiet Der Synthese von Kohlenwasserstoffen Aus CO Und H_2. *Chem. Ing. Tech.* **1970**, *42*, 1162−1174.
(46) Ciobîcă, I. M.; Kramer, G. J.; Ge, Q.; Neurock, M.; van Santen, R. A. Mechanisms for Chain Growth in Fischer−Tropsch Synthesis over Ru(0001). *J. Catal.* **2002**, *212*, 136−144.
(47) Wang, C.; Ekerdt, J. G. Evidence for Alkyl Intermediates during Fischer-Tropsch Synthesis and Their Relation to Hydrocarbon Products. *J. Catal.* **1984**, *86*, 239−244.
(48) Fernandes, F. A. N. Optimization of Fischer-Tropsch Synthesis Using Neural Networks. *Chem. Eng. Technol.* **2006**, *29*, 449−453.
(49) Demirbas, A. Converting Biomass Derived Synthetic Gas to Fuels via Fisher-Tropsch Synthesis. *Energy Sources, Part A* **2007**, *29*, 1507−1512.
(50) Kang, S.-H.; Bae, J. W.; Woo, K.-J.; Sai Prasad, P. S.; Jun, K.-W. ZSM-5 Supported Iron Catalysts for Fischer−Tropsch Production of Light Olefin. *Fuel Process. Technol.* **2010**, *91*, 399−403.
(51) Schulz, H.; van Steen, E.; Claeys, M. Specific Inhibition as the Kinetic Principle of the Fischer-Tropsch Synthesis. *Top. Catal.* **1995**, *2*, 223−234.
(52) Schulz, H.; Schaub, G.; Claeys, M.; Riedel, T. Transient Initial Kinetic Regimes of Fischer-Tropsch Synthesis. *Appl. Catal., A* **1999**, *186*, 215−227.
(53) Schulz, H.; Nie, Z.; Claeys, M. *Initial Episodes of Fischer-Tropsch Synthesis with Cobalt Catalysts*; Elsevier Masson SAS, 1998; Vol. *119*.
(54) Henrici-Olivé, G.; Olivé, S. The Fischer-Tropsch Synthesis: Molecular Weight Distribution of Primary Products and Reaction Mechanism. *Angew. Chem., Int. Ed. Engl.* **1976**, *15*, 136−141.
(55) Xiao, C.-x.; Cai, Z.-p.; Wang, T.; Kou, Y.; Yan, N. Aqueous-Phase Fischer−Tropsch Synthesis with a Ruthenium Nanocluster Catalyst. *Angew. Chem.* **2008**, *120*, 758−761.
(56) Peng, X.; Cheng, K.; Kang, J.; Gu, B.; Yu, X.; Zhang, Q.; Wang, Y. Impact of Hydrogenolysis on the Selectivity of the Fischer-Tropsch Synthesis: Diesel Fuel Production over Mesoporous Zeolite-Y-Supported Cobalt Nanoparticles. *Angew. Chem., Int. Ed.* **2015**, *54*, 4553−4556.
(57) Bartolini, M.; Molina, J.; Alvarez, J.; Goldwasser, M.; Pereira Almao, P.; Zurita, M. J. P. Effect of the Porous Structure of the Support on Hydrocarbon Distribution in the Fischer-Tropsch Reaction. *J. Power Sources* **2015**, *285*, 1−11.
(58) Subramanian, V.; Zholobenko, V. L.; Cheng, K.; Lancelot, C.; Heyte, S.; Thuriot, J.; Paul, S.; Ordomsky, V. V.; Khodakov, A. Y. The Role of Steric Effects and Acidity in the Direct Synthesis of Iso-Paraffins from Syngas on Cobalt Zeolite Catalysts. *ChemCatChem* **2016**, *8*, 380−389.
(59) Subramanian, V.; Cheng, K.; Lancelot, C.; Heyte, S.; Paul, S.; Moldovan, S.; Ersen, O.; Marinova, M.; Ordomsky, V. V.; Khodakov, A. Y. Nanoreactors: An Efficient Tool to Control the Chain-Length Distribution in Fischer-Tropsch Synthesis. *ACS Catal.* **2016**, *6*, 1785−1792.
(60) Zeng, B.; Hou, B.; Jia, L.; Li, D.; Sun, Y. Fischer-Tropsch Synthesis over Different Structured Catalysts: The Effect of Silica Coating onto Nanoparticles. *J. Mol. Catal. A: Chem.* **2013**, *379*, 263−268.
(61) Xie, R.; Li, D.; Hou, B.; Wang, J.; Jia, L.; Sun, Y. Solvothermally Derived Co_3O_4@m-SiO_2 Nanocomposites for Fischer-Tropsch Synthesis. *Catal. Commun.* **2011**, *12*, 380−383.
(62) Claeys, M.; Van Steen, E. On the Effect of Water during Fischer-Tropsch Synthesis with a Ruthenium Catalyst. *Catal. Today* **2002**, *71*, 419−427.
(63) King, D. Fischer-Tropsch Study of Supported Ruthenium Catalysts. *J. Catal.* **1978**, *51*, 386−397.
(64) Vannice, M. A. The Catalytic Synthesis of Hydrocarbons from Carbon Monoxide and Hydrogen. *Catal. Rev.* **1976**, *14*, 153−191.
(65) Vannice, M. The Catalytic Synthesis of Hydrocarbons from H_2/CO Mixtures over the Group VIII Metals II. The Kinetics of the Methanation Reaction over Supported Metals. *J. Catal.* **1975**, *37*, 462−473.
(66) Dry, M. E. Fischer-Tropsch Synthesis over Iron Catalysts. *Catal. Lett.* **1991**, *7*, 241−251.
(67) van Dijk, W. L.; Niemantsverdriet, J. W.; van dar Kraan, A. M.; van der Baan, H. S. Effects of Manganese Oxide and Sulphate on the Olefin Selectivity of Iron Catalysts in the Fischer Tropsch Reaction. *Appl. Catal.* **1982**, *2*, 273−288.
(68) Torres Galvis, H. M.; Bitter, J. H.; Khare, C. B.; Ruitenbeek, M.; Dugulan, A. I.; de Jong, K. P. Supported Iron Nanoparticles as Catalysts for Sustainable Production of Lower Olefins. *Science* **2012**, *335*, 835−838.
(69) Torres Galvis, H. M.; Koeken, A. C. J.; Bitter, J. H.; Davidian, T.; Ruitenbeek, M.; Dugulan, A. I.; De Jong, K. P. Effects of Sodium and Sulfur on Catalytic Performance of Supported Iron Catalysts for the Fischer-Tropsch Synthesis of Lower Olefins. *J. Catal.* **2013**, *303*, 22−30.
(70) Lu, Y.; Yan, Q.; Han, J.; Cao, B.; Street, J.; Yu, F. Fischer−Tropsch Synthesis of Olefin-Rich Liquid Hydrocarbons from Biomass-Derived Syngas over Carbon-Encapsulated Iron Carbide/Iron Nanoparticles Catalyst. *Fuel* **2017**, *193*, 369−384.
(71) Cheng, Y.; Lin, J.; Xu, K.; Wang, H.; Yao, X.; Pei, Y.; Yan, S.; Qiao, M.; Zong, B. Fischer-Tropsch Synthesis to Lower Olefins over Potassium-Promoted Reduced Graphene Oxide Supported Iron Catalysts. *ACS Catal.* **2016**, *6*, 389−399.
(72) Todic, B.; Nowicki, L.; Nikacevic, N.; Bukur, D. B. Fischer−Tropsch Synthesis Product Selectivity over an Industrial Iron-Based Catalyst: Effect of Process Conditions. *Catal. Today* **2016**, *261*, 28−39.
(73) Tau, L. M.; Dabbagh, H. A.; Davis, B. H. Fischer-Tropsch Synthesis: ^{14}C Tracer Study of Alkene Incorporation. *Energy Fuels* **1990**, *4*, 94−99.
(74) Gorimbo, J.; Lu, X.; Liu, X.; Hildebrandt, D.; Glasser, D. A Long Term Study of the Gas Phase of Low Pressure Fischer-Tropsch Products When Reducing an Iron Catalyst with Three Different Reducing Gases. *Appl. Catal., A* **2017**, *534*, 1−11.
(75) Arakawa, H.; Bell, A. T. Effects of Potassium Promotion on the Activity and Selectivity of Iron Fischer-Tropsch Catalysts. *Ind. Eng. Chem. Process Des. Dev.* **1983**, *22*, 97−103.
(76) Lox, E. S.; Froment, G. F. Kinetics of the Fischer-Tropsch Reaction on a Precipitated Promoted Iron Catalyst. 2. Kinetic Modeling. *Ind. Eng. Chem. Res.* **1993**, *32*, 71−82.
(77) Hla, S.; Park, D.; Duffy, G.; Edwards, J.; Roberts, D.; Ilyushechkin, A.; Morpeth, L.; Nguyen, T. Kinetics of High-Temperature Water-Gas Shift Reaction over Two Iron-Based Commercial Catalysts Using Simulated Coal-Derived Syngases. *Chem. Eng. J.* **2009**, *146*, 148−154.
(78) Bukur, D. B.; Todic, B.; Elbashir, N. Role of Water-Gas-Shift Reaction in Fischer−Tropsch Synthesis on Iron Catalysts: A Review. *Catal. Today* **2016**, *275*, 66−75.
(79) Zhu, M.; Wachs, I. E. Iron-Based Catalysts for the High-Temperature Water-Gas Shift (HT-WGS) Reaction: A Review. *ACS Catal.* **2016**, *6*, 722−732.
(80) Van Der Laan, G. P.; Beenackers, A. A. C. M. Intrinsic Kinetics of the Gas-Solid Fischer-Tropsch and Water Gas Shift Reactions over a Precipitated Iron Catalyst. *Appl. Catal., A* **2000**, *193*, 39−53.
(81) Natesakhawat, S.; Wang, X.; Zhang, L.; Ozkan, U. S. Development of Chromium-Free Iron-Based Catalysts for High-Temperature Water-Gas Shift Reaction. *J. Mol. Catal. A: Chem.* **2006**, *260*, 82−94.
(82) Huff, G. A.; Satterfield, C. N. Intrinsic Kinetics of the Fischer-Tropsch Synthesis on a Reduced Fused-Magnetite Catalyst. *Ind. Eng. Chem. Process Des. Dev.* **1984**, *23*, 696−705.

https://doi.org/10.1021/acs.jpcc.1c00254
J. Phys. Chem. C 2021, 125, 11891−11903

(83) Zimmerman, W. H.; Bukur, D. B. Reaction Kinetics over Iron Catalysts Used for the Fischer-Tropsch Synthesis. *Can. J. Chem. Eng.* **1990**, *68*, 292−301.
(84) Newsome, D. S. The Water-Gas Shift Reaction. *Catal. Rev.* **1980**, *21*, 275−318.
(85) Yates, I. C.; Satterfield, C. N. Intrinsic Kinetics of the Fischer-Tropsch Synthesis on a Cobalt Catalyst. *Energy Fuels* **1991**, *5*, 168−173.
(86) Chu, W.; Chernavskii, P.; Gengembre, L.; Pankina, G.; Fongarland, P.; Khodakov, A. Cobalt Species in Promoted Cobalt Alumina-Supported Fischer-Tropsch Catalysts. *J. Catal.* **2007**, *252*, 215−230.
(87) Saib, A. M.; Moodley, D. J.; Ciobîcă, I. M.; Hauman, M. M.; Sigwebela, B. H.; Weststrate, C. J.; Niemantsverdriet, J. W.; Van De Loosdrecht, J. Fundamental Understanding of Deactivation and Regeneration of Cobalt Fischer-Tropsch Synthesis Catalysts. *Catal. Today* **2010**, *154*, 271−282.
(88) Navarro, V.; Van Spronsen, M. A.; Frenken, J. W. M. In Situ Observation of Self-Assembled Hydrocarbon Fischer-Tropsch Products on a Cobalt Catalyst. *Nat. Chem.* **2016**, *8*, 929−934.
(89) Saib, A. M.; Claeys, M.; Van Steen, E. Silica Supported Cobalt Fischer-Tropsch Catalysts: Effect of Pore Diameter of Support. *Catal. Today* **2002**, *71*, 395−402.
(90) Riedel, T.; Claeys, M.; Schulz, H.; Schaub, G.; Nam, S.-S.; Jun, K.-W.; Choi, M.-J.; Kishan, G.; Lee, K.-W. Comparative Study of Fischer-Tropsch Synthesis with H_2/CO and H_2/CO_2 Syngas Using Fe- and Co-Based Catalysts. *Appl. Catal., A* **1999**, *186*, 201−213.
(91) Schulz, H.; Claeys, M. Reactions of α-Olefins of Different Chain Length Added during Fischer-Tropsch Synthesis on a Cobalt Catalyst in a Slurry Reactor. *Appl. Catal., A* **1999**, *186*, 71−90.
(92) Chaumette, P.; Courty, P.; Kiennemann, A.; Ernst, B. Higher Alcohol and Paraffin Synthesis on Cobalt Based Catalysts: Comparison of Mechanistic Aspects. *Top. Catal.* **1995**, *2*, 117−126.
(93) Van Der Laan, G. P.; Beenackers, A. A. C. M. Kinetics and Selectivity of the Fischer-Tropsch Synthesis: A Literature Review. *Catal. Rev.: Sci. Eng.* **1999**, *41*, 255−318.
(94) Ernst, B.; Bensaddik, A.; Hilaire, L.; Chaumette, P.; Kiennemann, A. Study on a Cobalt Silica Catalyst during Reduction and Fischer−Tropsch Reaction: In Situ EXAFS Compared to XPS and XRD. *Catal. Today* **1998**, *39*, 329−341.
(95) Bezemer, G. L.; Bitter, J. H.; Kuipers, H. P. C. E.; Oosterbeek, H.; Holewijn, J. E.; Xu, X.; Kapteijn, F.; van Dillen, A. J.; De Jong, K. P. Cobalt Particle Size Effects in the Fischer-Tropsch Reaction Studied with Carbon Nanofiber Supported Catalysts. *J. Am. Chem. Soc.* **2006**, *128*, 3956−3964.
(96) Govender, S.; Gambu, T. G.; van Heerden, T.; van Steen, E. Mechanistic Pathways for Oxygen Removal on Pt-Doped Co(111) in the Fischer-Tropsch Reaction. *Catal. Today* **2020**, *342*, 142−151.
(97) van Helden, P.; Berg, J.-A. v. d.; Petersen, M. A.; Janse van Rensburg, W.; Ciobîcă, I. M.; van de Loosdrecht, J. Computational Investigation of the Kinetics and Mechanism of the Initial Steps of the Fischer−Tropsch Synthesis on Cobalt. *Faraday Discuss.* **2017**, *197*, 117−151.
(98) Zheng, J.; Cai, J.; Jiang, F.; Xu, Y.; Liu, X. Investigation of the Highly Tunable Selectivity to Linear α-Olefins in Fischer-Tropsch Synthesis over Silica-Supported Co and CoMn Catalysts by Carburization-Reduction Pretreatment. *Catal. Sci. Technol.* **2017**, *7*, 4736−4755.
(99) Kresse, G.; Hafner, J. Ab Initio Molecular Dynamics for Liquid Metals. *Phys. Rev. B: Condens. Matter Mater. Phys.* **1993**, *47*, 558−561.
(100) Kresse, G.; Hafner, J. Ab Initio Molecular-Dynamics Simulation of the Liquid-Metal−Amorphous-Semiconductor Transition in Germanium. *Phys. Rev. B: Condens. Matter Mater. Phys.* **1994**, *49*, 14251−14269.
(101) Kresse, G.; Furthmüller, J. Efficient Iterative Schemes for Ab Initio Total-Energy Calculations Using a Plane-Wave Basis Set. *Phys. Rev. B: Condens. Matter Mater. Phys.* **1996**, *54*, 11169−11186.
(102) Kresse, G.; Furthmüller, J. Efficiency of Ab-Initio Total Energy Calculations for Metals and Semiconductors Using a Plane-Wave Basis Set. *Comput. Mater. Sci.* **1996**, *6*, 15−50.
(103) Perdew, J. P.; Burke, K.; Ernzerhof, M. Generalized Gradient Approximation Made Simple. *Phys. Rev. Lett.* **1996**, *77*, 3865−3868.
(104) Perdew, J. P.; Burke, K.; Ernzerhof, M. Generalized Gradient Approximation Made Simple [Phys. Rev. Lett. 77, 3865 (1996)]. *Phys. Rev. Lett.* **1997**, *78*, 1396.
(105) Blöchl, P. E. Projector Augmented-Wave Method. *Phys. Rev. B: Condens. Matter Mater. Phys.* **1994**, *50*, 17953−17979.
(106) Kresse, G.; Joubert, D. From Ultrasoft Pseudopotentials to the Projector Augmented-Wave Method. *Phys. Rev. B: Condens. Matter Mater. Phys.* **1999**, *59*, 1758−1775.
(107) Dudarev, S. L.; Botton, G. A.; Savrasov, S. Y.; Humphreys, C. J.; Sutton, A. P. Electron-Energy-Loss Spectra and the Structural Stability of Nickel Oxide: An LSDA+U Study. *Phys. Rev. B: Condens. Matter Mater. Phys.* **1998**, *57*, 1505−1509.
(108) Anisimov, V. I.; Korotin, M. A.; Zaanen, J.; Andersen, O. K. Spin Bags, Polarons, and Impurity Potentials in $La_{2-x}Sr_xCuO_4$ from First Principles. *Phys. Rev. Lett.* **1992**, *68*, 345−348.
(109) Farkaš, B.; Santos-Carballal, D.; Cadi-Essadek, A.; de Leeuw, N. H. A DFT+U Study of the Oxidation of Cobalt Nanoparticles: Implications for Biomedical Applications. *Materialia* **2019**, *7*, 100381.
(110) Cadi-Essadek, A.; Roldan, A.; Santos-Carballal, D.; Ngoepe, P. E.; Claeys, M.; de Leeuw, N. H. DFT+U Study of the Electronic, Magnetic, and Mechanical Properties of Co, CoO, and Co_3O_4. *South African J. Chem.* **2021**. in press.
(111) Grimme, S.; Antony, J.; Ehrlich, S.; Krieg, H. A Consistent and Accurate Ab Initio Parametrization of Density Functional Dispersion Correction (DFT-D) for the 94 Elements H-Pu. *J. Chem. Phys.* **2010**, *132*, 154104.
(112) Grimme, S.; Ehrlich, S.; Goerigk, L. Effect of the Damping Function in Dispersion Corrected Density Functional Theory. *J. Comput. Chem.* **2011**, *32*, 1456−1465.
(113) Postica, V.; Vahl, A.; Santos-Carballal, D.; Dankwort, T.; Kienle, L.; Hoppe, M.; Cadi-Essadek, A.; de Leeuw, N. H.; Terasa, M.-I.; Adelung, R.; et al. Tuning ZnO Sensors Reactivity toward Volatile Organic Compounds via Ag Doping and Nanoparticle Functionalization. *ACS Appl. Mater. Interfaces* **2019**, *11*, 31452−31466.
(114) Posada-Pérez, S.; Santos-Carballal, D.; Terranova, U.; Roldan, A.; Illas, F.; de Leeuw, N. H. CO2 interaction with violarite (FeNi2S4) surfaces: a dispersion-corrected DFT study. *Phys. Chem. Chem. Phys.* **2018**, *20*, 20439−20446.
(115) Ungerer, M. J.; Santos-Carballal, D.; Cadi-Essadek, A.; van Sittert, C. G. C. E.; de Leeuw, N. H. Interaction of H2O with the Platinum Pt (001), (011), and (111) Surfaces: A Density Functional Theory Study with Long-Range Dispersion Corrections. *J. Phys. Chem. C* **2019**, *123*, 27465−27476.
(116) Postica, V.; Vahl, A.; Strobel, J.; Santos-Carballal, D.; Lupan, O.; Cadi-Essadek, A.; De Leeuw, N. H.; Schütt, F.; Polonskyi, O.; Strunskus, T.; et al. Tuning Doping and Surface Functionalization of Columnar Oxide Films for Volatile Organic Compounds Sensing: Experiments and Theory. *J. Mater. Chem. A* **2018**, *6*, 23669−23682.
(117) Ramogayana, B.; Santos-Carballal, D.; Aparicio, P. A.; Quesne, M. G.; Maenetja, K. P.; Ngoepe, P. E.; de Leeuw, N. H. Ethylene carbonate adsorption on the major surfaces of lithium manganese oxide Li1−xMn2O4spinel (0.000. *Phys. Chem. Chem. Phys.* **2020**, *22*, 6763−6771.
(118) Watson, G. W.; Kelsey, E. T.; de Leeuw, N. H.; Harris, D. J.; Parker, S. C. Atomistic Simulation of Dislocations, Surfaces and Interfaces in MgO. *J. Chem. Soc. Faraday Trans.* **1996**, *92*, 433−438.
(119) Monkhorst, H. J.; Pack, J. D. Special Points for Brillouin-Zone Integrations. *Phys. Rev. B: Solid State* **1976**, *13*, 5188−5192.
(120) Methfessel, M.; Paxton, A. T. High-Precision Sampling for Brillouin-Zone Integration in Metals. *Phys. Rev. B: Condens. Matter Mater. Phys.* **1989**, *40*, 3616−3621.
(121) Mermin, N. D. Thermal Properties of the Inhomogeneous Electron Gas. *Phys. Rev.* **1965**, *137*, A1441−A1443.

https://doi.org/10.1021/acs.jpcc.1c00254
J. Phys. Chem. C 2021, 125, 11891−11903

(122) Blöchl, P. E.; Jepsen, O.; Andersen, O. K. Improved Tetrahedron Method for Brillouin-Zone Integrations. *Phys. Rev. B: Condens. Matter Mater. Phys.* **1994**, *49*, 16223−16233.
(123) Makov, G.; Payne, M. C. Periodic Boundary Conditions in Ab Initio Calculations. *Phys. Rev. B: Condens. Matter Mater. Phys.* **1995**, *51*, 4014−4022.
(124) Neugebauer, J.; Scheffler, M. Adsorbate-Substrate and Adsorbate-Adsorbate Interactions of Na and K Adlayers on Al(111). *Phys. Rev. B: Condens. Matter Mater. Phys.* **1992**, *46*, 16067−16080.
(125) Henkelman, G.; Arnaldsson, A.; Jónsson, H. A Fast and Robust Algorithm for Bader Decomposition of Charge Density. *Comput. Mater. Sci.* **2006**, *36*, 354−360.
(126) Sanville, E.; Kenny, S. D.; Smith, R.; Henkelman, G. Improved Grid-Based Algorithm for Bader Charge Allocation. *J. Comput. Chem.* **2007**, *28*, 899−908.
(127) Tang, W.; Sanville, E.; Henkelman, G. A Grid-Based Bader Analysis Algorithm without Lattice Bias. *J. Phys.: Condens. Matter* **2009**, *21*, 084204.
(128) Tersoff, J.; Hamann, D. R. Theory of the Scanning Tunneling Microscope. *Phys. Rev. B: Condens. Matter Mater. Phys.* **1985**, *31*, 805−813.
(129) Vanpoucke, D. E. P.; Brocks, G. Formation of Pt-Induced Ge Atomic Nanowires on Pt/Ge(001): A Density Functional Theory Study. *Phys. Rev. B: Condens. Matter Mater. Phys.* **2008**, *77*, 241308.
(130) Henkelman, G.; Uberuaga, B. P.; Jónsson, H. A Climbing Image Nudged Elastic Band Method for Finding Saddle Points and Minimum Energy Paths. *J. Chem. Phys.* **2000**, *113*, 9901−9904.
(131) Henkelman, G.; Jónsson, H. Improved Tangent Estimate in the Nudged Elastic Band Method for Finding Minimum Energy Paths and Saddle Points. *J. Chem. Phys.* **2000**, *113*, 9978−9985.
(132) Sheppard, D.; Terrell, R.; Henkelman, G. Optimization Methods for Finding Minimum Energy Paths. *J. Chem. Phys.* **2008**, *128*, 134106.
(133) Nocedal, J. Updating Quasi-Newton Matrices with Limited Storage. *Math. Comput.* **1980**, *35*, 773.
(134) Chase, M. W. J. *NIST JANAF Thermochemical Tables*; American Chemical Society and American Institute of Physics for the National Institute of Standards and Technology: Washington DC, 1998.
(135) Wang, X.-G.; Weiss, W.; Shaikhutdinov, S.; Ritter, M.; Petersen, M.; Wagner, F.; Schlögl, R.; Scheffler, M. The Hematite (α-Fe_2O_3) (0001) Surface: Evidence for Domains of Distinct Chemistry. *Phys. Rev. Lett.* **1998**, *81*, 1038−1041.
(136) Santos-Carballal, D.; Roldan, A.; Grau-Crespo, R.; de Leeuw, N. H. A DFT Study of the Structures, Stabilities and Redox Behaviour of the Major Surfaces of Magnetite Fe_3O_4. *Phys. Chem. Chem. Phys.* **2014**, *16*, 21082−21097.
(137) Marick, L. Variation of Resistance and Structure of Cobalt with Temperature and a Discussion of Its Photoelectric Emission. *Phys. Rev.* **1936**, *49*, 831−837.
(138) Taylor, A.; Floyd, R. W. Precision Measurements of Lattice Parameters of Non-Cubic Crystals. *Acta Crystallogr.* **1950**, *3*, 285−289.
(139) Bucher, J. P.; Douglass, D. C.; Bloomfield, L. A. Magnetic Properties of Free Cobalt Clusters. *Phys. Rev. Lett.* **1991**, *66*, 3052−3055.
(140) Moruzzi, V. L.; Marcus, P. M.; Schwarz, K.; Mohn, P. Total Energy Surfaces in the M-V Plane for Bcc and Fcc Cobalt. *J. Magn. Magn. Mater.* **1986**, *54*−*57*, 955−956.
(141) Min, B. I.; Oguchi, T.; Freeman, A. J. Structural, Electronic, and Magnetic Properties of Co: Evidence for Magnetism-Stabilizing Structure. *Phys. Rev. B: Condens. Matter Mater. Phys.* **1986**, *33*, 7852−7854.
(142) Bagayoko, D.; Ziegler, A.; Callaway, J. Band Structure of Bcc Cobalt. *Phys. Rev. B: Condens. Matter Mater. Phys.* **1983**, *27*, 7046−7049.
(143) Respaud, M.; Broto, J. M.; Rakoto, H.; Fert, A. R.; Thomas, L.; Barbara, B.; Verelst, M.; Snoeck, E.; Lecante, P.; Mosset, A.; et al. Surface Effects on the Magnetic Properties of Ultrafine Cobalt Particles. *Phys. Rev. B: Condens. Matter Mater. Phys.* **1998**, *57*, 2925−2935.
(144) Santos-Carballal, D.; Roldan, A.; Grau-Crespo, R.; de Leeuw, N. H. First-principles study of the inversion thermodynamics and electronic structure ofFeM2X4(thio)spinels (M=Cr, Mn, Co, Ni;X=O, S). *Phys. Rev. B: Condens. Matter Mater. Phys.* **2015**, *91*, 195106.
(145) Santos-Carballal, D.; Ngoepe, P. E.; de Leeuw, N. H. Ab Initio Investigation of the Thermodynamics of Cation Distribution and of the Electronic and Magnetic Structures in the $LiMn_2O_4$ Spinel. *Phys. Rev. B* **2018**, *97*, 085126.
(146) Skriver, H. L.; Rosengaard, N. M. Surface Energy and Work Function of Elemental Metals. *Phys. Rev. B: Condens. Matter Mater. Phys.* **1992**, *46*, 7157−7168.
(147) Aldén, M.; Mirbt, S.; Skriver, H. L.; Rosengaard, N. M.; Johansson, B. Surface Magnetism in Iron, Cobalt, and Nickel. *Phys. Rev. B: Condens. Matter Mater. Phys.* **1992**, *46*, 6303−6312.
(148) Huber, K. P.; Herzberg, G. *Molecular Spectra and Molecular Structure*; Springer US: Boston, MA, 1979.
(149) Beckel, C. L.; Shafi, M.; Engelke, R. Comparison of Actual and Linearly Extrapolated Dissociation Energies of Diatomic Molecules. *J. Mol. Spectrosc.* **1971**, *40*, 519−535.
(150) Santos-Carballal, D.; Roldan, A.; de Leeuw, N. H. Early Oxidation Processes on the Greigite Fe_3S_4(001) Surface by Water: A Density Functional Theory Study. *J. Phys. Chem. C* **2016**, *120*, 8616−8629.
(151) Santos-Carballal, D.; Roldan, A.; Dzade, N. Y.; de Leeuw, N. H. Reactivity of CO 2 on the surfaces of magnetite (Fe 3 O 4), greigite (Fe 3 S 4) and mackinawite (FeS). *Philos. Trans. R. Soc. A Math. Phys. Eng. Sci.* **2018**, *376*, 20170065.
(152) Santos-Carballal, D.; Roldan, A.; de Leeuw, N. H. CO_2 reduction to acetic acid on the greigite Fe_3S_4{111} surface. *Faraday Discuss.* **2021**, DOI: 10.1039/C9FD00141G. in press